The Astrophysical Journal, 969:136 (8pp), 2024 July 10 https://doi.org/10.3847/1538-4357/ad50a9

AT2021lwx: Another Neutrino-coincident Tidal Disruption Event with a Strong Dust Echo?

Chengchao Yuan (袁成超)[1], Walter Winter[1], and Cecilia Lunardini[2]
[1] Deutsches Elektronen-Synchrotron DESY, Platanenallee 6, 15738 Zeuthen, Germany; chengchao.yuan@desy.de
[2] Department of Physics, Arizona State University, 450 E. Tyler Mall, Tempe, AZ 85287-1504, USA

Received 2024 January 22; revised 2024 May 22; accepted 2024 May 23; published 2024 July 9

Abstract

We discuss the possible association of an astrophysical neutrino (IC220405B) with the recently reported, extremely energetic tidal disruption event (TDE) candidate AT2021lwx (ZTF20abrbeie, aka "Scary Barbie") at redshift $z = 0.995$. Although the TDE is about $2\overset{\circ}{.}6$ off the direction of the reconstructed neutrino event (outside the 90% confidence level localization region), the TDE candidate shares some important characteristics with so-far-reported neutrino–TDE associations: a strong infrared dust echo, high bolometric luminosity, a neutrino time delay with respect to the peak mass accretion rate of the order of a hundred days, and a high observed X-ray luminosity. We interpret this new association using an isotropic emission model, where neutrinos are produced by the collision of accelerated protons with infrared photons. After accounting for the high redshift of AT2021lwx (by interpreting the data in the supermassive black hole (SMBH) frame), we find that the expected neutrino fluences and neutrino time delays are qualitatively comparable to the other TDEs. Since data are only available up to 300 days postpeak in the SMBH frame, significant uncertainties exist in the dust echo interpretation, and therefore in the predicted number of neutrinos detected, $\mathcal{N}_\nu \simeq 3.0 \times 10^{-3} - 0.012$. We recommend further follow-up of this object for an extended period and suggest refining the reconstruction of the neutrino arrival direction in this particular case.

Unified Astronomy Thesaurus concepts: Tidal disruption (1696); Radiative processes (2055); Neutrino astronomy (1100); High energy astrophysics (739)

1. Introduction

Tidal disruption events (TDEs) are energetic optical transients that originate from stars that are tidally destroyed as they transit within the tidal radius of a supermassive black hole (SMBH). Approximately half of the stellar mass remains bound, and its subsequent accretion could power an electromagnetic (EM) flare that lasts from months to years (Rees 1988; Phinney 1989). Nowadays, increasingly detailed multiwavelength observations of TDEs by the Zwicky Transient Facility (ZTF; Bellm et al. 2019), the Wide-field Infrared Survey Explorer (WISE; Wright et al. 2010), and X-ray/radio surveys, such as eROSITA (Sazonov et al. 2021) and the Very Large Array Sky Survey (Lacy et al. 2020), facilitate comprehensive modeling of the radiation processes and cosmological distributions of this source population (e.g., van Velzen et al. 2021; Hammerstein et al. 2023; Yao et al. 2023).

Among the hundred or so observed TDEs and TDE candidates, three have been found to be coincident—in time and position—with three IceCube astrophysical neutrino events. They include an event that was classified as a TDE with high confidence, AT2019dsg (Stein et al. 2021), and two TDE candidates, AT2019fdr (Reusch et al. 2022) and AT2019aalc (van Velzen et al. 2024), with associated neutrinos IC191001A, IC200530A, and IC19119A, respectively. These three candidate neutrino emitters share some prominent similarities. For instance, they all exhibit high optical–ultraviolet (OUV) luminosities accompanied by bright and delayed infrared (IR) emissions, which have been interpreted as dust echoes, i.e., reprocessed radiation from the OUV and X-ray bands into IR wavelengths by surrounding dust (Jiang et al. 2016; Lu et al. 2016; van Velzen et al. 2016). These three TDEs are located within the 90% confidence limit (CL) localization region of the corresponding neutrino events (Abbasi et al. 2023), with an angular deviation $\Delta\theta \sim 1\overset{\circ}{.}3$–$1\overset{\circ}{.}9$ (van Velzen et al. 2024). The neutrino events were detected with significant time delays—approximately 150–300 days—after the OUV peak in the observer's frame.

These three neutrino–TDE associations identify TDEs as potential cosmic-ray accelerators, as neutrinos are a by-product of hadronic processes. Many models including relativistic jets (Wang et al. 2011; Wang & Liu 2016; Dai & Fang 2017; Lunardini & Winter 2017; Senno et al. 2017), accretion disks (Hayasaki & Yamazaki 2019), wide-angle outflows/hidden winds (Fang et al. 2020), and tidal stream interactions (Dai et al. 2015; Hayasaki & Yamazaki 2019) have been proposed as the origin of the nonthermal EM and neutrino emissions from TDEs, which could potentially explain these TDE–neutrino coincidences. Some models also offer a physical explanation of the observed neutrino time delays (Liu et al. 2020; Murase et al. 2020; Hayasaki 2021; Winter & Lunardini 2021; Wu et al. 2022; Mukhopadhyay et al. 2023; Winter & Lunardini 2023). In the context of multimessenger astrophysics, TDE parameters and neutrino detectability can be constrained using X-ray or γ-ray upper bounds (see, e.g., Yuan & Winter 2023, for the application to AT2019dsg and AT2019fdr).

Recently, two additional dust-obscured TDE candidates, exhibiting strong dust echo signatures, were reported to be spatially and temporally coincident with Gold-type (the chance of astrophysical origin is larger than 50%) astrophysical neutrinos events at IceCube (Jiang et al. 2023).

Here, we point out the potential coincidence between another energetic TDE candidate, AT2021lwx (ZTF20abrbeie, aka "Scary Barbie"), and an IceCube neutrino event, IC220405B (Necker et al. 2022). Noting that AT2021lwx is not within the 90% CL area of the neutrino event, and IC220405B is classified as a Bronze-type neutrino alert (where the chance of astrophysical origin is larger than 30%), the probability of the neutrino correlation with AT2021lwx is lower than the candidates mentioned before. However, AT2021lwx shares some prominent signatures with other neutrino-coincident TDEs and candidates, encompassing a strong dust echo which explains the IR observations, high bolometric OUV and X-ray luminosities, and a comparable time delay of the neutrino detection. These similarities suggest that AT2021lwx may be another member of a class of neutrino-emitting TDEs, for which a common underlying mechanism exists. In this context, it is interesting to investigate the neutrino correlations and multimessenger implications.

In this paper, we offer an interpretation of AT2021lwx in terms of a model where neutrinos and EM cascade emissions originate from accelerated protons colliding with IR target photons, similar to the one presented in Winter & Lunardini (2023) and Yuan & Winter (2023, model "M-IR" therein). We first discuss the likelihood of the neutrino correlation in Section 2.1. Given the crucial role of the IR radiation, in Section 2.2, we fit the IR light curve using an early-time (ET) component in addition to a delayed component produced by the spherical dust torus, and discuss the uncertainties arising from the absence of late-time IR data. In Section 3, we further employ an isotropic wind model, constructed based on OUV–IR–X-ray observations, as described in Winter & Lunardini (2023) and Yuan & Winter (2023), to investigate the spectral and temporal signatures of neutrino and EM cascade emissions produced within the dust radius. In addition, we compare AT2021lwx to AT2019dsg/fdr/aalc in terms of bolometric OUV and IR luminosities, as well as predicted neutrino fluences, and discuss the γ-ray constraints and the likelihood of producing one neutrino event at IceCube in Section 4.

2. AT2021lwx

2.1. Localization of AT2021lwx and IC220405B

Motivated by the similarities among the neutrino-coincident TDE candidates, here we investigate the potential spatial and temporal coincidence between AT2021lwx and IC220405B (Necker et al. 2022). AT2021lwx was initially discovered by ZTF on 2021 April 13 and was classified as a TDE candidate at redshift of $z = 0.995$ (Subrayan et al. 2023). The peak bolometric optical luminosity, after correcting for extinction, is exceptionally high, reaching 10^{46} erg s^{-1}. Multiwavelength follow-ups have revealed bright X-ray and IR emissions (Wiseman et al. 2023). The latter has been preliminarily interpreted as a dust echo. We point out one Bronze-type neutrino alert, IC220405B,[3] which is close to the TDE direction with an angular offset of $\Delta\theta \simeq 2.^{\circ}6$, and arrived approximately 370 days after the OUV peak, equivalent to $\sim$185 days in the SMBH rest frame.

Figure 1 depicts the locations of AT2021lwx and IC220405B. We obtain the 2σ and 3σ containment areas of the neutrino event by performing a Gaussian extrapolation of the 90% CL box[4] (the dashed red rectangular; Necker et al. 2022) and applying a systematic uncertainty in the arrival direction of $\sigma_{\rm sys} = 1.^{\circ}0$ motivated by the estimates in IceCube Collaboration (2013) and Plavin et al. (2020).

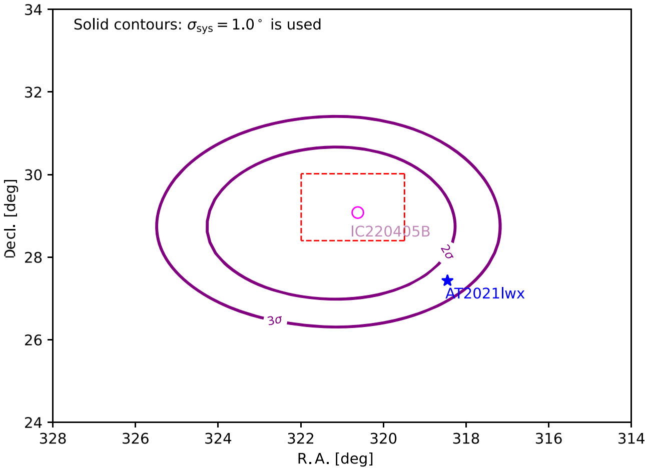

Figure 1. Localization of IC220405B and AT2021lwx. The red dashed rectangular shows the 90% CL containment region of IC220405B (Necker et al. 2022). The inner and outer purple contours correspond to the 2σ and 3σ containment areas obtained by taking into account the systematic uncertainty $\sigma_{\rm sys} = 1.0^{\circ}$.

We find that AT2021lwx locates in the 3σ containment contour in the refined localization analysis. Caution must be exercised when establishing the significance of the association since it is inferred from the initial 90% CL localization box, and a more precise localization constraint requires detailed point-source (PS) reconstructions from the IceCube Collaboration.

2.2. Dust Echo Modeling

Modeling of ZTF photometry indicates that AT2021lwx was produced by the tidal disruption of a massive star of $M_\star \sim 14$ $M_\odot$ by an SMBH of $M_{\rm BH} \sim 10^8$ $M_\odot$ (Subrayan et al. 2023). However, it is important to note that this object is not exclusively identified as a TDE, given the low likelihood of such an event involving a massive star. At first, it was classified as a flare from an active galactic nucleus (AGN; Grayling et al. 2022); another plausible interpretation is an unusually powerful accretion of a giant molecular cloud by an SMBH of 10^8–10^9 $M_\odot$ (Wiseman et al. 2023). Nevertheless, the classification does not significantly influence our multimessenger modeling, since our model ingredients, such as the proton injection rate and target photon fields, are built on the OUV–IR–X-ray observations, including the light curves and the spectra.

For AT2021lwx, the IR light curve was measured by WISE in the W1 and W2 bands before and after the OUV peak. The IR data points in the upper panel of Figure 2 and the OUV light curve of AT2021lwx are taken from Subrayan et al. (2023) and Wiseman et al. (2023), respectively, following bolometric corrections. The OUV and IR spectra are consistent with blackbody distributions and the temperatures are measured to be $T_{\rm OUV} \sim 1.2$–1.6×10^4 K (1.03–1.38 eV) and $T_{\rm IR} \sim 10^3$ K (0.9 eV) in the SMBH rest frame (Subrayan et al. 2023;

---

[3] This neutrino event was initially named as IC220405A (IceCube Collaboration 2022).

[4] More specifically, we derive the Gaussian standard deviations for each side of the rectangle using the corresponding 90% CL uncertainties and then employ a two-dimensional Gaussian distribution to obtain the contours. Note that the positional error is statistical only; there is no systematic added.

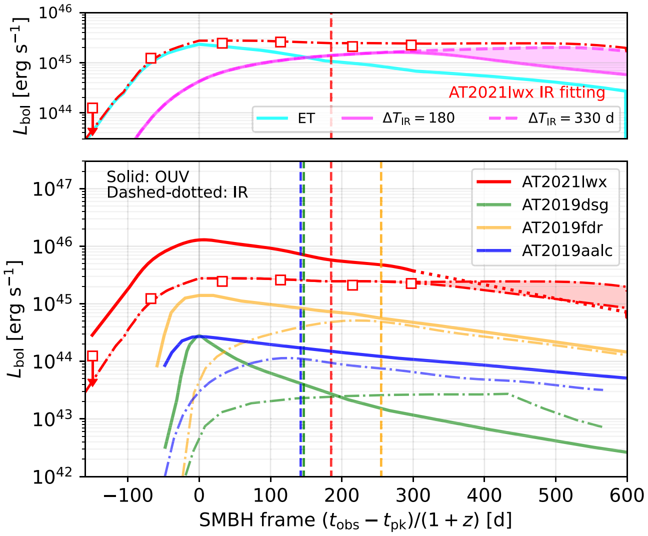

Figure 2. Upper panel: IR light-curve interpretation for AT2021lwx in the SMBH frame. The IR bolometric luminosity derived from WISE W1 and W2 light curves (Wiseman et al. 2023) are shown as the square dots. The ET and spherical dust torus components are depicted respectively as the cyan and magenta curves, whereas the red dashed–dotted curve is the total IR luminosity. The magenta area corresponding to the uncertainties of the IR time delay, e.g., $\Delta T_{\rm IR} = 180-330$ days. Lower panel: bolometric OUV (solid curves) and IR (dashed–dotted curves) light curves of AT2021lwx and the other three neutrino-coincident TDEs (Winter & Lunardini 2023) in the SMBH frame. The vertical dashed lines show the detection times of the corresponding neutrino events.

Wiseman et al. 2023). Using these temperatures, we calculate the bolometric correction factors, defined as the ratio of the energy flux from the entire blackbody spectrum to the energy flux in the r, g, W1, and W2 bands. From that, we then obtain the OUV and IR bolometric luminosities, denoted as $L_{\rm OUV}$ and $L_{\rm IR}$, respectively. We stress that here $L_{\rm OUV}$ is corrected for extinction, as will be clear from the derivation in the remainder of this section. The red square markers in Figure 2 show $L_{\rm IR}$ as inferred from WISE measurements, as a function of the time in SMBH rest frame, e.g., $(t_{\rm obs} - t_{\rm pk})/(1+z)$, where $t_{\rm obs}$ is the time in the observer's frame and $t_{\rm pk}$ is the time that OUV luminosity peaks. The red solid curve in the lower panel represents $L_{\rm OUV}$ for the time interval where data exist; its extrapolation to later times is shown as a red dotted curve. We find the peak values of $L_{\rm OUV}$ and $L_{\rm IR}$ to be $\simeq 1.2 \times 10^{46}$ erg s^{-1} and $\simeq 3.1 \times 10^{45}$ erg s^{-1}, respectively. Our bolometric OUV luminosity, $L_{\rm OUV}$, is roughly a factor of ~ 2 higher than the value in Subrayan et al. (2023) since we corrected it for absorption by ambient dust, which induces the dust echo. This correction will be introduced at the end of this section.

The first impression we obtain from Figure 2 is that AT2021lwx exhibits a comparable neutrino time delay with the other three TDEs in the SMBH frame (see the vertical lines in Figure 2), and its flat/steady IR luminosity after the OUV peak is consistent with a dust echo. This dust echo interpretation is supported by the measured IR temperature, $T_{\rm IR} \sim 10^3$ K, which is below the dust sublimation temperature of $T_{\rm sub} \sim 1800$ K (van Velzen et al. 2016).

We neglect the contribution of X-rays to the dust echo as was done in Winter & Lunardini (2023) since the X-ray emission was first observed more than 300 days after the OUV peak by the Swift X-ray Telescope (XRT) and the unabsorbed luminosity was inferred to be $L_X \sim 1.5 \times 10^{45}$ erg s^{-1} $\ll L_{\rm OUV}$ (Wiseman et al. 2023).

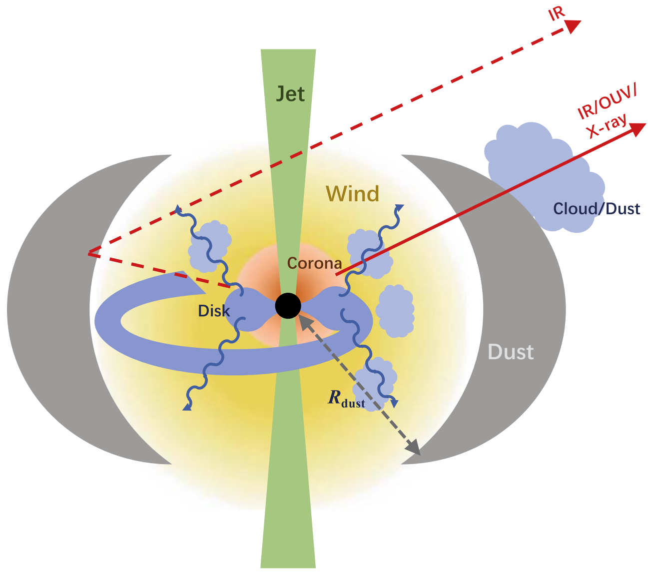

Figure 3. Schematic picture of the dust echo model. The central SMBH, accretion stream, accretion disk, disk corona, wind, dust torus, and potentially a jet are shown. To fit the IR light curve, we model the dust torus as a spherical segment (e.g., the dashed red lines) and consider an additional ET component (e.g., the red solid line). The physical origins of the ET component are discussed in the main text. The radius of dust torus $R_{\rm dust}$ determines the IR time delay.

To fit the bolometric IR luminosity, we model $L_{\rm IR}$ as the convolution of $L_{\rm OUV}$ with a (normalized) time-spreading function $f(t)$, which depends on the spatial distribution of the surrounding dust (Reusch et al. 2022; Winter & Lunardini 2023):

$$L_{\rm IR}(t) = \epsilon_{\rm dust}\,\epsilon_\Omega \int_{-\infty}^{+\infty} L_{\rm OUV}(t') f(t - t') dt', \tag{1}$$

where $\epsilon_{\rm dust} < 1$ represents the fraction of the incident radiation that is reprocessed to IR radiation by the illuminated dust, and ϵ_Ω is the solid angle coverage factor of the dust distribution. Our chosen form of $f(t)$ is inspired from the IR light curve in Figure 2. We notice that, unlike AT2019dsg/fdr/aalc, whose IR emissions are very weak before the OUV peak, for AT2021lwx the IR light curve seems to have a component that evolves like $L_{\rm OUV}$ at early times. The late-time evolutions of $L_{\rm IR}$ and $L_{\rm OUV}$ suggest that the former may eventually overtake the latter, and persist over a longer timescale. These considerations lead to a two-component model of the echo, where the ET component is attributed to either anisotropic dust distribution or preexisting dust around the SMBH (with no time delay with respect to $L_{\rm OUV}$), whereas the late-time part is attributed to a dust torus similar to those of AT2019dsg/fdr/aalc.

Figure 3 schematically illustrates the physical picture of the spherical and ET components of the dust echo, where the SMBH, accretion disk, disk corona, isotropic wind envelope, dust torus, and potentially a jet are shown. The red dashed lines indicate the optical paths that cause the time delay of the dust torus component due to the extended dust torus. Observationally, $2\Delta T_{\rm IR}$ is comparable with the IR time delay defined as the time difference between the IR and OUV peaks in the SMBH frame, with which we can infer the radius of the inner edge of dust torus, i.e., $R_{\rm dust} \simeq c\Delta T_{\rm IR}$. An external dust cloud,

Table 1
Physical Parameters of AT2021lwx

Description	**Parameter**	**Value**
Redshift	z	0.995
OUV peak time (MJD)	$t_{\rm pk}$	59291
SMBH mass ($M_\odot$)	$M_{\rm BH}$	10^8
Star mass ($M_\odot$)	$M_\star$	14
Peak accretion rate	$\dot{M}_{\rm BH}(t_{\rm pk})$	$40 L_{\rm Edd}/c^2$
Neutrino Observation	IC220405B	
Detection time (day)	$t_\nu - t_{\rm pk}$	$\sim$370
Energy (TeV)	E_ν	106
Angular deviation (deg)	$\Delta\theta$	2.6
Dust Echo Modeling		
Dust echo efficiency	$\epsilon_\Omega \epsilon_{\rm dust}$	0.32 (0.43)
ET weighting	λ	0.4 (0.3)
IR time dispersion (day)	$\Delta T_{\rm IR}$	180 (330)
Dust torus radius (cm)	$R_{\rm dust}$	5.4×10^{17} (10^{18})
Proton efficiency	ε_p	0.2
Max proton energy (GeV)	$E_{p,\rm max}$	1.5×10^9
Magnetic field (G)	B	0.1

Note. The numbers in parentheses correspond to the case of a longer time delay of $\Delta T_{\rm IR} = 330$ days (magenta dashed line in Figure 2). Data references: z, $t_{\rm pk}$, $M_{\rm BH}$, and $M_\star$ (Subrayan et al. 2023); and t_ν and E_ν (Necker et al. 2022). The dust echo efficiency $\epsilon_\Omega \epsilon_{\rm dust}$ is assumed to be compatible with Winter & Lunardini (2023).

responsible for the undelayed component of $L_{\rm IR}$, is also shown in the figure. Formally, in the function $f(t)$, the ET component is represented by a Dirac Delta, $f_{\rm ET}(t) = \delta(t)$, whereas the torus component can be represented by the commonly used box function (see, e.g., Reusch et al. 2022): $f_{\rm S}(t) = 1/(2\Delta T_{\rm IR})$ if $0 \leqslant t \leqslant 2\Delta T_{\rm IR}$ otherwise $f_{\rm S}(t) = 0$. Combining $f_{\rm ET}$ and $f_{\rm S}$, we explicitly write down the normalized time-spreading function:

$$f(t) = f_{\rm ET} + f_{\rm S} = \lambda\delta(t) + \frac{(1-\lambda)}{2\Delta T_{\rm IR}} H(t, 0, 2\Delta T_{\rm IR}), \quad (2)$$

where the weighting parameter $0 \leqslant \lambda \leqslant 1$ represents the fraction of total IR power that can be attributed to line-of-sight dust, and $H(x, a, b)$ is a step function, e.g., $H(x, a, b) = 1$ if $a < x < b$ otherwise $H(x, a, b) = 0$.

We assume an overall dust echo efficiency $\epsilon_{\rm dust}\epsilon_\Omega \simeq 0.3-0.4$, comparable to Winter & Lunardini (2023), and use Equations (1) and (2) to explain the bolometric IR light curve. Combining $\epsilon_{\rm dust}\epsilon_\Omega$ and ET weighting factor λ, we infer the dust echo efficiencies for the ET component and the spherical dust torus component, respectively, as $\lambda\epsilon_{\rm dust}\epsilon_\Omega$ and $(1-\lambda)\epsilon_{\rm dust}\epsilon_\Omega$. The best-fit values of λ and $\Delta T_{\rm IR}$ are given in Table 1, whereas the best-fit IR light curves are shown in the upper panel of Figure 2. Since the IR data are only available up to 300 days after the OUV peak and the IR light curve maintains a flat shape until the latest data point, the IR time delay is, therefore, uncertain, which is illustrated by the shaded magenta area. The solid magenta line predicts the immediate decrease after the latest data point, e.g., $\Delta T_{\rm IR} = 180$ days, while the dashed–dotted magenta line corresponds to a more extended dust torus $R_{\rm dust} \sim 10^{18}$ cm as reported in Wiseman et al. (2023). Table 1 lists the dust echo parameters from the IR interpretation. The dust radius is estimated to be $R_{\rm dust} = c\Delta T_{\rm IR} \sim 5.4 \times 10^{17}-10^{18}$ cm and is consistent with the dust sublimation radius (e.g., Namekata & Umemura 2016; Jiang et al. 2019):

$$R_{\rm sub} \simeq 6.3 \times 10^{17}\ {\rm cm}\ L_{\rm IR,\,45.5}^{1/2} T_{\rm sub,\,3.25}^{-2.8} a_{\rm dust,-5}^{-0.51}, \quad (3)$$

where $L_{\rm IR,45.5} = L_{\rm IR}/(10^{45.5}\ {\rm erg\ s^{-1}})$, $T_{\rm sub} \simeq 1800$ K is the sublimation temperature, and $a_{\rm dust} \sim 10^{-5} a_{\rm dust,-5}$ cm is the dust grain radius.

Figure 2 demonstrates that our two-component model can explain the IR observations very well and could be tested by further IR follow-ups. However, we need to note that based on the current observations, our fitting suggests that a static spherical dust torus is not sufficient to explain the whole IR light curve, and we cannot exclusively determine the physical meaning of the ET component. For instance, it could arise from an anisotropic or irregular dust distribution, or from preexisting dust clumps around the SMBH (e.g., Jiang et al. 2019), as shown in Figure 3. Another possibility is an expanding dust torus pushed by radiation or winds, which introduces the time evolution of the dust compared to a static distribution described by $f_{\rm S}$. A detailed study of the physical interpretation of $f_{\rm ET}$ is beyond the scope of this work. In the following text, we use our two-component fitting to describe the evolution of IR target photons for neutrino production. Our IR light curve can be considered as an "effective" description that reproduces the data well. Different physical scenarios—if they fit the data well—should give a similar light curve. Therefore, our IR model is sufficient for the purpose of this study.

Using the dust echo efficiency $\epsilon_{\rm dust}\epsilon_\Omega$ in Table 1, we can estimate the IR-corrected OUV bolometric energy $\mathcal{E}_{\rm OUV} \approx \mathcal{E}_{\rm IR}/(\epsilon_{\rm dust}\,\epsilon_\Omega) \sim 0.3\, M_\odot c^2 \simeq \int L_{\rm OUV}\, dt$, where $\mathcal{E}_{\rm IR} \sim 0.1 - 0.13\, M_\odot c^2$ is the IR bolometric energy obtained by integrating $L_{\rm IR}$ over time. From this chain of equations, and assuming that the absorbed and unabsorbed OUV luminosities have the same time dependence, we finally obtain $L_{\rm OUV}$. One caveat in our IR interpretation is the assumption of $\epsilon_{\rm dust}\epsilon_\Omega$, which renders the unabsorbed $L_{\rm OUV}$ model dependent. Nevertheless, we will demonstrate later that the IR photons would dominate the neutrino and EM cascade emissions, and our conclusions do not depend sensitively on $\epsilon_{\rm dust}\epsilon_\Omega$.

3. Neutrino and Electromagnetic Cascade Emissions

The observational parameters for AT2021lwx and the potentially associated neutrino event IC220405B are summarized in Table 1. We follow the treatments in Winter & Lunardini (2023) and Yuan & Winter (2023) and assume the injected proton luminosity is a fraction of the accretion power, e.g., $L_p = \varepsilon_p \dot{M}_{\rm BH} c^2$, where an efficient proton injection efficiency $\varepsilon_p = 0.2$ is used as the fiducial value as in Winter & Lunardini (2023) for AT2019dsg/fdr/aalc. We assume the accretion rate aligns with the OUV light curve, e.g., $\dot{M}_{\rm BH} \propto L_{\rm OUV}$ as it is consistent with the $t^{-5/3}$ prediction, which reflects the accretion history. The peak accretion rate[5] $\dot{M}_{\rm BH}(t_{\rm pk}) = 40 L_{\rm Edd}/c^2$ is estimated to avoid exceeding the hard upper limit of the accreted mass $\int \dot{M}_{\rm BH} dt \lesssim M_\star/2$, where $L_{\rm Edd} = 1.3 \times 10^{46}$ erg s^{-1}($M_{\rm BH}/10^8\ M_\odot$) is the Eddington luminosity. On the other hand, the peak accretion rate can be interpreted as super-Eddington accretion with $\dot{M}_{\rm BH}(t_{\rm pk})/\dot{M}_{\rm Edd} = \mathcal{O}(1.0)$, where the Eddington accretion rate

---

[5] Note that in Winter & Lunardini (2023), the highly super-Eddington peak accretion rate, $\dot{M}_{\rm BH}(t_{\rm pk}) = 100 L_{\rm Edd}/c^2$, is used.

$\dot{M}_{\rm Edd} = L_{\rm Edd}/(\eta_{\rm rad} c^2)$ indicates the accretion rate to power Eddington radiation with the radiation efficiency $\eta_w \sim 0.01-0.1$ (McKinney et al. 2015). Our IR-corrected OUV bolometric peak luminosity reaches $\sim 1.2 \times 10^{46}$ erg s^{-1} and is comparable with the Eddington luminosity $L_{\rm Edd} = 1.3 \times 10^{46}$ erg s^{-1} for an SMBH of mass $M_{\rm BH} = 10^8$ $M_\odot$. In this case, the peak mass accretion rate can reach a few × 10 $L_{\rm Edd}/c^2$ with $\dot{M}_{\rm BH}(t_{\rm pk})/\dot{M}_{\rm Edd} = 1$ and $\eta_{\rm rad} \sim 0.01-0.1$. Hence, our fiducial $\dot{M}_{\rm BH}(t_{\rm pk}) = 40 L_{\rm Edd}/c^2$ is not too optimistic.

We assume a power-law injection rate for the accelerated protons in the isotropic wind region inside the dust torus, e.g., $Q_p \propto E_p^{-2} \exp(-E_p/E_{p,\rm max})$ and normalize the spectrum with $\int E \dot{Q}_p dE_p = L_p/V$, where $V \approx 4\pi R_{\rm dust}^3/3$ is the volume within the dust.[6] Without explicitly specifying the accelerator, we instead parameterize the acceleration zone by the maximal proton energy $E_{p,\rm max}$. In general, the protons can be energized in the compact inner jet, accretion disk or disk corona, or an extended isotropic wind (e.g., Murase et al. 2020) with a magnetic field strength comparable to AGNs, e.g., $B \sim 0.1$–1 G.

While propagating inside the radiation zone (the yellow region in Figure 3), the protons will undergo photomeson (p–γ) and hadronuclear (p–p) energy losses via interactions, respectively, with target thermal photons and wind protons. The resulting neutral (π^0) and charged ($\pi^\pm$) pions would decay into neutrinos, γ-rays, and secondary electrons. These secondary electrons together with the electron–positron pairs generated from γ–γ annihilation and Bethe–Heitler (B-H) interactions will subsequently initiate EM cascade emissions via synchrotron and inverse Compton radiation. We denote the EM cascade components originating from the p–γ, γ–γ, and B-H processes, respectively, as "pg-syic," "pair-syic," and "bh-syic." To obtain the neutrino and EM cascade spectra, we use the Astrophysical Multi-Messenger Modeling (Gao et al. 2017; Klinger et al. 2023) software to numerically solve the coupled time-dependent transport equations for all relevant particle species; see Yuan & Winter (2023) for a detailed description and discussion of the transport equations, including the particle injection, energy loss, and escape terms.

As demonstrated by Winter & Lunardini (2023) and Yuan & Winter (2023), the contribution to neutrino and EM cascade emissions from p–p interactions is typically subdominant compared to the p–γ processes, even if a significant fraction of the accreted mass is converted to nonrelativistic winds with velocities of $0.1c$ (Dai et al. 2018; Yuan et al. 2020, 2021). In the following text, we specifically focus on the p–γ contributions. For the target photon fields, we consider the thermal IR, OUV, and X-ray photons isotropized within the dust radius. Since the ET component in the IR light-curve interpretation could be produced by dust outside the radiation zone, as shown in Figure 3, we consider only the dust torus component for the IR target photons, i.e., the magenta curves in the upper panel of Figure 2, in a conservative case. For the X-ray component, we assume a constant luminosity of $L_{\rm X} = 1.5 \times 10^{45}$ erg s^{-1} as in Winter & Lunardini (2023) and use an AT2019dsg-like temperature of $k_{\rm B} T_{\rm X} = 72$ eV. We use a magnetic field strength $B = 0.1$ G as the fiducial value as in Winter & Lunardini (2023).

Figure 4 shows the proton energy loss rates (left panel) and the neutrino/EM cascade spectral energy distributions (SEDs; right panel) produced in the isotropic wind of radius $R_{\rm dust}$ at neutrino detection time t_ν. We assume the maximum energy of the injected proton to be 1.5×10^9 GeV. In the left panel, the red, green, orange, and black curves, respectively, depict the p–γ, B-H, proton synchrotron, and escape rates. The horizontal gray lines show the free streaming rates ($t_{\rm f.s.}^{-1} = c/R_{\rm dust}$) for neutral particles. The cases of shorter and longer IR time dispersion, e.g., $\Delta T_{\rm IR} = 180$ and 330 days, respectively, are shown as the dashed and solid curves. In both cases, the p–γ interactions are efficient and fast in the proton energy range $E_p \sim 10^7-10^9$ GeV, e.g., $t_{p\gamma}^{-1}/t_{\rm f.s.}^{-1} > 1$, which implies that the neutrino radiation is mainly constrained by the proton luminosity. Given the acceleration efficiency $\eta_{\rm acc} \lesssim 1$, the proton acceleration rates, $t_{p,\rm acc}^{-1} = \eta_{\rm acc} eBc/E_p$, are illustrated as blue lines. Despite $E_{p,\rm max}$ being treated as a free parameter without specifying the acceleration sites, we demonstrate that $E_{p,\rm max} = 1.5 \times 10^9$ GeV is achievable within the wind (one possible site for proton acceleration) for the magnetic field $B = 0.1$ G. The red circles in the left panel demonstrate that the chosen $E_{p,\rm max}$ can be obtained for reasonable/conservative acceleration efficiencies $\eta_{\rm acc} = 0.3$ and 1.0 for the IR time spreads $\Delta T_{\rm IR} = 330$ days and 180 days, respectively, from balancing the acceleration rate with the proton interaction rate.

The right panel of Figure 4 shows the SEDs for target photons (magenta curves), overall EM cascades (black curves), and neutrinos (red curves). The dashed and solid curves have the same meaning as in the left panel. For the shorter IR time delay case ($\Delta T_{\rm IR} = 180$ days), the orange, green, and blue curves illustrate the contributions from secondary electrons/positrons originated from γ–γ annihilation, p–γ, and B-H processes, respectively. The γ-rays from π^0 decays are completely depleted via γ–γ annihilation with in-source thermal photons and extragalactic background light. A more detailed and quantitative description of the EM cascade SEDs can be found in Yuan & Winter (2023). The orange and cyan areas depict the Swift-XRT and Fermi-Large Area Telescope (LAT) energy ranges. The nondetection of γ-rays by Fermi-LAT in the direction of IC220405B places an upper limit on the energy range 0.1−800 GeV (Garrappa et al. 2022), shown as the cyan upper limit. We find that our results are consistent with the observational constraints even for the optimistic parameter sets.

Comparisons of the predicted neutrino fluence, obtained by integrating the flux and neutrino luminosity in the SMBH frame of AT2021lwx with AT2019dsg/fdr/aalc, are illustrated in the left and right panels of Figure 5. The red areas correspond to the uncertainties from the IR interpretations, e.g., $\Delta T_{\rm IR} = 180$–330 days and $R_{\rm dust} = 5.4 \times 10^{17}-10^{18}$ cm. The IceCube sensitivities for PS (Aartsen et al. 2014) and γ-ray follow-up (GFU; Blaufuss et al. 2019) searches are plotted as the thin gray dashed–dotted curves. We observe that the neutrino spectra of AT2021lwx are similar to those of the other three TDEs but at a lower fluence level due to the high redshift. Using the GFU effective area,[7] we estimate the expected

---

[6] In Yuan & Winter (2023), the more compact radiation zones, where thermal OUV photons dominate the p–γ interactions, are discussed as well. However, for AT2019lwx, a smaller radius (10^{16}–10^{17} cm) would lead to very bright EM cascade emission, which would contradict the nondetection of γ-rays by the Fermi-Large Area Telescope (LAT); this scenario is therefore omitted.

[7] The GFU neutrino numbers, estimated using the IceCube GFU effective areas (IceCube Collaboration et al. 2016), are more suitable when comparing the model predictions to actual follow-up observations, whereas PS neutrino numbers are typically used for independent PS analyses.

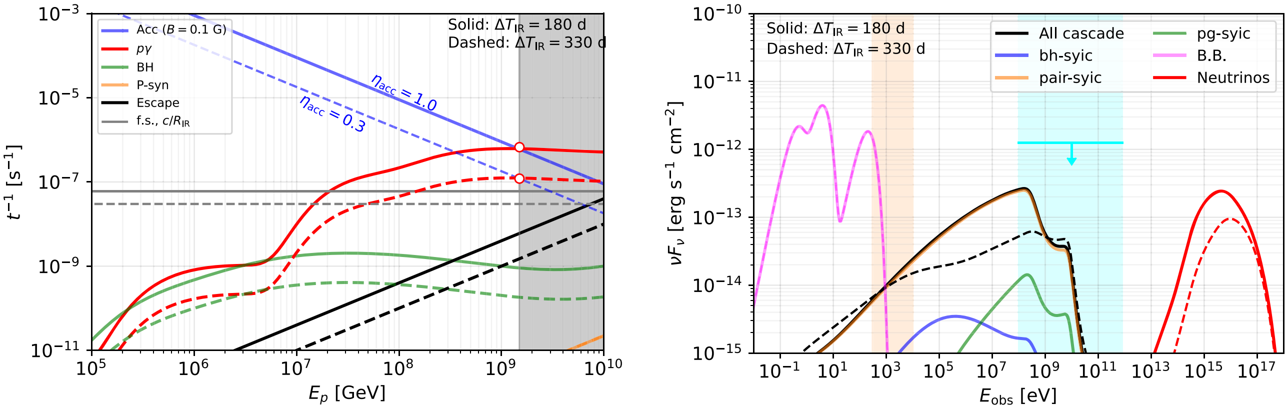

Figure 4. Left panel: in-source interaction rates shown at the neutrino detection time t_ν. The solid and dashed curves correspond to the shorter ($\Delta T_{\rm IR} = 180$ days) and longer ($\Delta T_{\rm IR} = 330$ days) IR time delays, respectively, with different assumptions for $R_{\rm dust}$. The gray shaded area shows the region beyond the maximum proton energy, whereas the acceleration efficiencies, $\eta_{\rm acc} = 1.0{-}0.3$ can be used to describe $E_{p,\rm max}$, see the red circles. Right panel: SED of the muon neutrino (red curves) and EM cascade (black curves) emissions at the neutrino detection time. The magenta curve shows the spectrum of target blackbody photons. The dashed and solid curves have the same meaning as in the left panel. For the $\Delta T = 180$ day case, the orange, green, and blue dashed curves represent the components of EM cascades. The orange and cyan areas depict the XRT and Fermi-LAT energy ranges, respectively, whereas the Fermi upper limit is shown as the cyan arrow.

neutrino number from AT2021lwx to be in the range of $\mathcal{N}_\nu \simeq 3.0 \times 10^{-3} - 0.012$, which is lower than the other three TDEs. From the right panel, the peak time of the neutrino luminosity of AT2021lwx, e.g., 100–200 days in the SMBH frame, could explain the time delay of IC220405B (vertical red dashed line).

4. Discussion

Let us first of all note that the description of the IR emission is a crucial part in our scenario, because the chosen maximal proton energies reaching $E_{p,\rm max} \simeq 10^9$ GeV allow for p–γ interactions beyond the threshold with the abundant IR photons—which are dominating the neutrino and accompanying EM cascade emissions. Moreover, the radius of the dust torus, which determines the target photon density and consequently the p–γ interaction efficiency, can be inferred from the time delay in the IR light curves, defined as the time difference between the OUV and IR peaks. We propose an interpretation of the IR light curve that consists of a spherical dust torus and an ET component, denoted as $f_{\rm S}$ and $f_{\rm ET}$, respectively.

The primary uncertainty in the multimessenger modeling of AT2021lwx arises from the lack of IR data since 300 days after the OUV peak in the SMBH frame, which leads to the uncertainties in the evaluation of the time delay, the time dispersion $\Delta T_{\rm IR}$ of the dust torus component (the magenta curves in Figure 2 and the $f_{\rm S}$ term in Equation (2)), and equivalently the radius $R_{\rm dust} = c\Delta T_{\rm IR}$. Our IR interpretation demonstrates that the time dispersion (~half of the time delay in the SMBH frame) lies in the range $\Delta T_{\rm IR} \simeq 180$–330 days, which corresponds to a dust radius $R_{\rm dust} = c\Delta T_{\rm IR} \simeq (5.4\text{–}10) \times 10^{17}$ cm. The resulting uncertainties in the neutrino and EM emissions are illustrated in Figures 4 and 5, and the predicted neutrino number is limited to be $\mathcal{N}_\nu \simeq 3 \times 10^{-3} - 0.12$. Further follow-up observations up to $2(1+z)\Delta T_{\rm IR} \sim 1300$ days after the OUV peak are advisable to obtain more stringent constraints on the neutrino number and on our model.

On the other hand, a two-component dust echo scenario is constructed to interpret the ET IR light curve. There could be other alternative models, such as dust clumps in the broad-line regions of TDEs in AGNs (Jiang et al. 2019) or bounded/unbounded debris. If the early IR emissions are produced within the dust radius (i.e., our radiation zone), one should take these IR photons (inferred from the cyan curve in the upper panel of Figure 2) into account as additional targets for the p–γ interactions. We tested for a potential additional contribution of ET IR photons and found that the neutrino fluence is affected by a factor less than 1.5. The reason is that the system is already p–γ efficient, and the neutrino power is limited by the injected proton luminosity, which is determined by $\varepsilon_p \dot{M}_{\rm BH}(t_{\rm pk})$ and is also constrained by the Fermi-LAT upper limit.

Our multimessenger model, which gives $\mathcal{N}_\nu \lesssim 0.012$, seems to disfavor the neutrino–TDE coincidence together with the misalignment of the TDE outside the neutrino 90% error box. However, aside from the similarities with AT2019dsg/fdr/aalc and the potential correlation with IC220405B, AT2021lwx remains an important TDE candidate, being one of the nonjetted TDEs with the highest redshifts (see, e.g., Yao et al. 2023, for a TDE sample), and could have profound implication on the redshift distribution of TDEs, including the SMBH mass and the mass of the disrupted star. For AT2021lwx, the total energy released in the OUV bands reaches $\mathcal{E}_{\rm OUV} = \int L_{\rm OUV} dt \sim 0.3 M_\odot c^2$, which implies an accreted mass $M_{\rm acc} \sim \mathcal{E}_{\rm OUV}/(\eta_{\rm rad} c^2) \sim 3{-}30\ M_\odot$[8] given the radiation efficiency $\eta_{\rm rad} \sim 0.1$–0.01. Indeed, the volumetric rates, i.e., $\dot{\rho}_{{\rm TDE},\star}$, of TDEs with $M_{\rm BH} \sim 10^8\ M_\odot$ and $M_{\rm acc} \sim 3$–30 $M_\odot$ are low. On the other hand, given the high redshift of AT2021lwx, such detection is not impossible especially for a high cosmological volume if the event is bright enough. Considering a rapid redshift evolution, e.g., $\dot{\rho}_{{\rm TDE},\star} \propto (1+z)^{-3}$, we compare the relative TDE rate, i.e., $\dot{N}_{\rm TDE}(z < z_{\rm lim}) \sim V_{\rm co}(z_{\rm lim})\,\dot{\rho}_{{\rm TDE},\star}(z_{\rm lim})$, up to redshift $z_{\rm lim} = 0.995$ to the AT2019fdr-like redshift $z_{\rm lim} = 0.26$, $\dot{N}_{\rm TDE}(z < 0.995)/\dot{N}_{\rm TDE}(z < 0.26) \sim V_{\rm co}(0.995)/[4V_{\rm co}(0.26)] \sim 8$, where $V_{\rm co}(z)$ is the cosmological comoving volume at z. This implies that a powerful object involving a massive star has a larger abundance across large cosmological volumes. Similar results could be obtained using the TDE rate inferred from the star formation history and SMBH mass function (e.g., Kochanek 2016).

---

[8] Such estimation is based on the energy conversion and does not depend sensitively on the classification of AT2021lwx.

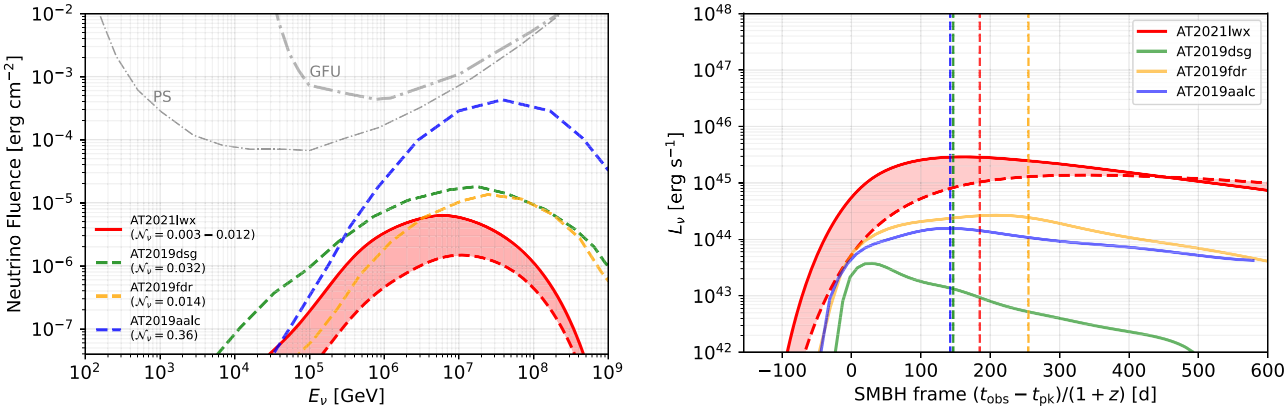

Figure 5. Left panel: cumulative single-flavor neutrino fluences at t_ν for AT2021lwx (red curves) and the other three TDEs, AT2019dsg/fdr/aalc (green/orange/blue dashed curves, taken from Winter & Lunardini 2023). The thin and thick dashed–dotted gray curves show the IceCube sensitivities for the PS and GFU searches, respectively. The uncertainties in the IR light-curve interpretation lead to the expected GFU neutrino number in the range $\mathcal{N}_\nu = 3 \times 10^{-3} - 0.012$. Right panel: neutrino luminosities for AT2021lwx and the other three TDEs measured in the SMBH frame. The vertical lines represent the corresponding neutrino detection times. The solid (dashed) curves correspond to $\Delta T_{\rm IR} = 180$ days (330 days), and the red areas correspond to the uncertainties from dust echo interpretations.

In addition to the IR photons, p–γ interactions with X-ray photons could also dominate neutrino production within a relatively compact radiation zone, as proposed by Winter & Lunardini (2023, their model "M-X"); this option is attractive because it requires much lower maximal proton energies, and, thus, a much less efficient accelerator. For AT2021lwx, due to the absence of ET X-ray observations and incomplete information about the radius of the X-ray emitters, we focus on the dust echo model and do not consider the scenario where X-rays are dominant.

5. Summary and Conclusions

We have investigated the potential correlation between the neutrino event IC220405B and an energetic TDE candidate, AT2021lwx, at redshift $z = 0.995$. In addition to luminous thermal OUV emissions, AT2021lwx exhibits bright and long-lasting IR luminosities, which can be interpreted as a strong dust echo incorporating dust torus and ET contributions. We have pointed out that AT2021lwx shares crucial similarities with the other three neutrino-coincident TDEs and TDE candidates, e.g., AT2019dsg/fdr/aalc, including strong X-ray and OUV emissions, strong dust echoes, and comparable time delays (∼150–300 days) of the neutrino detection with respect to the OUV peaks in the SMBH rest frame. We have studied the neutrino and EM cascade emissions from an isotropic radiation zone inside the dust radius in a fully time-dependent manner following the treatments in Winter & Lunardini (2023) and Yuan & Winter (2023). We have demonstrated that the outputs, such as the EM and neutrino SEDs, and neutrino light curves and fluences, are qualitatively consistent with the other three TDEs. Especially, the neutrino time delay could be explained by dust echo target photons. These similarities make AT2021lwx an interesting target and imply that these objects may share similar underlying physical processes.

Our results indicate that, in consistency with the nondetection of γ-rays by Fermi-LAT, the expected neutrino counts are limited to the range $\mathcal{N}_\nu \simeq 3.0 \times 10^{-3} - 0.012$, which is expected for faraway sources and might suggest that the association could have low significance. However, the expected event rate is not very different from the other three TDEs, and such low event rates are expected for single neutrino event detections from many faraway sources (Eddington bias; see Strotjohann et al. 2019).

We suggest conducting further multiwavelength follow-ups, especially in the IR band, on this object for an extended period. Additionally, we recommend studying the neutrino track reconstruction in this particular case for a more definitive conclusion regarding the neutrino correlation. Extended IR observations, such as the upcoming annual data release of the WISE survey, along with the confirmation or exclusion of the neutrino coincidence, would test our dust echo model and shed more light on the physical picture of TDEs, such as the geometry of the dust torus and the origin of the ET IR component. In all, our time-dependent multimessenger diagnosis, consisting of the neutrino and EM cascade counterparts, provides a comprehensive and generic template for interpreting the spectral and temporal signatures of future neutrino-coincident TDEs.

Note added: after the paper was submitted, the NEOWISE 2024 data were released, extending the IR light curve to MJD 60252, equivalent to approximately 481 days after the OUV peak in the SMBH rest frame. The latest data release[9] indicates that the late-time W1 and W2 apparent magnitudes remained roughly unchanged from the early epochs. We infer that the unbinned data points lie within the uncertainties of our model (e.g., the red areas in Figure 2). Refined analyses of the late-time IR data would be needed to obtain a robust constraint on $R_{\rm IR}$.

Acknowledgments

We would like to thank Simeon Reusch, Marek Kowalski, and Ning Jiang for useful discussions, and Xin-Yue Shi for a thorough internal review. C.L. acknowledges support from the NSF grant PHY-2309973, and from the National Astronomical Observatory of Japan, where part of this work was conducted.

ORCID iDs

Chengchao Yuan (袁成超) https://orcid.org/0000-0003-0327-6136
Walter Winter https://orcid.org/0000-0001-7062-0289
Cecilia Lunardini https://orcid.org/0000-0002-9253-1663

---

[9] The data are available at https://irsa.ipac.caltech.edu/frontpage/.

References

Aartsen, M. G., Ackermann, M., Adams, J., et al. 2014, ApJ, 796, 109

Abbasi, R., Ackermann, M., Adams, J., et al. 2023, ApJS, 269, 25

Bellm, E. C., Kulkarni, S. R., Graham, M. J., et al. 2019, PASP, 131, 018002

Blaufuss, E., Kintscher, T., Lu, L., & Tung, C. F. 2019, ICRC (Madison, WI), 36, 1021

Dai, L., & Fang, K. 2017, MNRAS, 469, 1354

Dai, L., McKinney, J. C., & Miller, M. C. 2015, ApJL, 812, L39

Dai, L., McKinney, J. C., Roth, N., Ramirez-Ruiz, E., & Miller, M. C. 2018, ApJL, 859, L20

Fang, K., Metzger, B. D., Vurm, I., Aydi, E., & Chomiuk, L. 2020, ApJ, 904, 4

Gao, S., Pohl, M., & Winter, W. 2017, ApJ, 843, 109

Garrappa, S., Buson, S. & Fermi-LAT Collaboration 2022, GCN, 31845, 1

Grayling, M., Toy, M., Wiseman, P., et al. 2022, TNSAN, 195, 1

Hammerstein, E., van Velzen, S., Gezari, S., et al. 2023, ApJ, 942, 9

Hayasaki, K. 2021, NatAs, 5, 436

Hayasaki, K., & Yamazaki, R. 2019, ApJ, 886, 114

IceCube Collaboration 2013, Sci, 342, 1242856

IceCube Collaboration 2022, GCN, 31839, 1

IceCube Collaboration, Aartsen, M. G., Abraham, K., et al. 2016, JInst, 11, P11009

Jiang, N., Dou, L., Wang, T., et al. 2016, ApJL, 828, L14

Jiang, N., Wang, T., Mou, G., et al. 2019, ApJ, 871, 15

Jiang, N., Zhou, Z., Zhu, J., Wang, Y., & Wang, T. 2023, ApJL, 953, L12

Klinger, M., Rudolph, A., Rodrigues, X., et al. 2023, arXiv:2312.13371

Kochanek, C. S. 2016, MNRAS, 461, 371

Lacy, M., Baum, S. A., Chandler, C. J., et al. 2020, PASP, 132, 035001

Liu, R.-Y., Xi, S.-Q., & Wang, X.-Y. 2020, PhRvD, 102, 083028

Lu, W., Kumar, P., & Evans, N. J. 2016, MNRAS, 458, 575

Lunardini, C., & Winter, W. 2017, PhRvD, 95, 123001

McKinney, J. C., Dai, L., & Avara, M. J. 2015, MNRAS, 454, L6

Mukhopadhyay, M., Bhattacharya, M., & Murase, K. 2023, arXiv:2309.02275

Murase, K., Kimura, S. S., Zhang, B. T., Oikonomou, F., & Petropoulou, M. 2020, ApJ, 902, 108

Namekata, D., & Umemura, M. 2016, MNRAS, 460, 980

Necker, J., Stein, R., Weimann, S., et al. 2022, GCN, 31842, 1

Phinney, E. S. 1989, in IAU Symp. 136, The Center of the Galaxy, ed. M. Morris (Dordrecht: Kluwer), 543

Plavin, A., Kovalev, Y. Y., Kovalev, Y. A., & Troitsky, S. 2020, ApJ, 894, 101

Rees, M. J. 1988, Natur, 333, 523

Reusch, S., Stein, R., Kowalski, M., et al. 2022, PhRvL, 128, 221101

Sazonov, S., Gilfanov, M., Medvedev, P., et al. 2021, MNRAS, 508, 3820

Senno, N., Murase, K., & Mészáros, P. 2017, ApJ, 838, 3

Stein, R., van Velzen, S., Kowalski, M., et al. 2021, NatAs, 5, 510

Strotjohann, N. L., Kowalski, M., & Franckowiak, A. 2019, A&A, 622, L9

Subrayan, B. M., Milisavljevic, D., Chornock, R., et al. 2023, ApJL, 948, L19

van Velzen, S., Gezari, S., Hammerstein, E., et al. 2021, ApJ, 908, 4

van Velzen, S., Mendez, A. J., Krolik, J. H., & Gorjian, V. 2016, ApJ, 829, 19

van Velzen, S., Stein, R., Gilfanov, M., et al. 2024, MNRAS, 529, 2559

Wang, X.-Y., & Liu, R.-Y. 2016, PhRvD, 93, 083005

Wang, X.-Y., Liu, R.-Y., Dai, Z.-G., & Cheng, K. S. 2011, PhRvD, 84, 081301

Winter, W., & Lunardini, C. 2021, NatAs, 5, 472

Winter, W., & Lunardini, C. 2023, ApJ, 948, 42

Wiseman, P., Wang, Y., Hönig, S., et al. 2023, MNRAS, 522, 3992

Wright, E. L., Eisenhardt, P. R. M., Mainzer, A. K., et al. 2010, AJ, 140, 1868

Wu, H.-J., Mou, G., Wang, K., Wang, W., & Li, Z. 2022, MNRAS, 514, 4406

Yao, Y., Ravi, V., Gezari, S., et al. 2023, ApJL, 955, L6

Yuan, C., Murase, K., Kimura, S. S., & Mészáros, P. 2020, PhRvD, 102, 083013

Yuan, C., Murase, K., Zhang, B. T., Kimura, S. S., & Mészáros, P. 2021, ApJL, 911, L15

Yuan, C., & Winter, W. 2023, ApJ, 956, 30